

# Hanle effect observations with the Ca I 4227 Å line

M. Bianda<sup>1</sup>, J.O. Stenflo<sup>2</sup>, and S.K. Solanki<sup>2</sup>

<sup>1</sup> Istituto Ricerche Solari Locarno (IRSOL), Via Patocchi, 6605 Locarno-Monti, Switzerland

<sup>2</sup> Institute of Astronomy, ETH Zentrum, 8092 Zürich, Switzerland (stenflo@astro.phys.ethz.ch)

Received 6 July 1999 / Accepted 10 September 1999

**Abstract.** The Hanle effect in the Ca I 4227 Å line has been explored through the analysis of a large number of Stokes profile recordings obtained on the quiet Sun with the beam-splitter polarimeter system at IRSOL (Istituto Ricerche Solari Locarno). In contrast to previous Hanle observations with this line, which were limited to the Stokes  $I$  and  $Q$  parameters, we are now in a position to study the combined effects of Hanle depolarization (via Stokes  $Q$ ) and rotation of the plane of linear polarization (via Stokes  $U$ ) with the same methods that we recently applied to the Sr II 4078 Å line. The Hanle histograms for the distributions of the depolarization and rotation parameters are very similar for the two lines and show that there must be mixed contributions to the Hanle signals from spatially unresolved magnetic fields with random orientations (which do not contribute to Stokes  $U$ ) and partially resolved magnetic fields with a net orientation of the field vectors. Field strengths in the range 5–10 G are preferred. We also determine the “Hanle efficiency profile”, which shows how the Hanle effect is confined to the Doppler core but vanishes in the line wings. It is wider than the corresponding profile for the Sr line, as expected from the difference in atomic weight and wavelength between the two lines. The  $Q/I$  profiles of the Ca I 4227 Å line have minima around the Doppler core which turn negative (polarization perpendicular to the limb) for limb distances  $\mu = \cos \theta \gtrsim 0.2$ , a likely signature of partial redistribution effects.

**Key words:** atomic processes – polarization – scattering – techniques: polarimetric – Sun: magnetic fields

## 1. Introduction

With the availability of high-precision imaging Stokes polarimeters it has become possible to make use of the Hanle effect as a new tool for magnetic-field diagnostics across the solar disk. The Hanle effect is sensitive to magnetic fields in a different parameter regime as compared with the Zeeman effect, in particular to weak fields, turbulent fields, and chromospheric fields. While the most sensitive polarimeter system ZIMPOL (Zurich Imaging Polarimeter, cf. Povel 1995) has been used to explore differential depolarization effects in various spectral lines due to the Hanle effect (Stenflo et al. 1998), the most

promising spectral region for Hanle diagnostics is in the blue and ultraviolet below the sensitivity limit of about 4500 Å for ZIMPOL.

As the only sufficiently sensitive imaging Stokes polarimeter for this spectral region is the beam-splitter system at IRSOL (Istituto Ricerche Solari Locarno), we have embarked on a program to use the versatile IRSOL facility for systematic explorations of scattering polarization physics, the Hanle effect, and associated magnetic-field diagnostics. The general observing and reduction technique was described in detail in Bianda et al. (1998a), here referred to as Paper I, in which we also studied the behavior of the Stokes  $I$  and  $Q$  profiles for the Ca I 4227 Å line and developed a method to determine the Hanle depolarization and corresponding field-strength values. In a subsequent work (Bianda et al. 1998b, here referred to as Paper II) we did a similar study for the Sr II 4078 Å line, but extended the observations and analysis to also include Stokes  $U$ , to allow us to determine the combined effects of Hanle depolarization and rotation of the plane of linear polarization. Histograms of different Hanle parameters were introduced as a new diagnostic tool for magnetic-field distributions in a regime inaccessible to the Zeeman effect. While Papers I and II exclusively dealt with the quiet Sun, observations of the full Stokes vector in active regions were presented in Bianda et al. (1999), here referred to as Paper III, which illustrated how the Hanle and Zeeman effects mix in the intermediate field regime, and how these polarization effects exhibit large spatial fluctuations on scales of a few arcsec or less.

In the present paper we return to the exploration of the Hanle effect in quiet regions in the Ca I 4227 Å line that was initiated in Paper I, but our new data set is richer and includes recordings of the Stokes  $U$  parameter, which allows us to explore for the Ca I line the combined effects of Hanle depolarization and rotation as was done for Sr II in Paper II. We also here introduce a method to determine the absolute zero point of the polarization scale and substantially improve the technique of accurately determining the  $\mu$  (cosine of the heliocentric angle) value used as the parameter for the center-to-limb distance. We can then construct histograms for the Hanle depolarization and rotation as well as for the field strength and also determine the efficiency profile that describes how the Hanle effect varies from line core to the wings.

*Send offprint requests to:* J.O. Stenflo

The results presented here agree closely with the corresponding results for the Sr II line in Paper II. This consistency between results obtained in different spectral lines places the Hanle-type interpretation of the observed polarization effects on firmer ground and also helps constrain the intrinsic field distributions on the Sun. Although we have converted the observed Hanle depolarizations to field-strength distributions (with maxima typically around 5–10 G), more detailed quantitative interpretations require numerical radiative-transfer modelling like that of Faurobert-Scholl (1992, 1994), but this is outside the scope of the present paper.

Because of our improved control of the true zero point of the polarization scale we are able to show how negative values of the  $Q/I$  polarization appear at the wavelengths, where we have a transition from the Doppler core to the dispersion wings, and the center-to-limb variation of these negative values, including their sign reversal near  $\mu \approx 0.2$ , are determined. Since these line frequencies are sensitive to the details of partial frequency redistribution of scattering polarization, these center-to-limb curves offer an interesting testing ground for radiative-transfer physics and may contain information of significant diagnostic value.

## 2. Observational and data reduction techniques

As in Papers I–III all our observations were carried out with the Semel-type polarimeter (cf. Semel et al. 1993; Semel 1995) and the Gregory-Coudé telescope at IRSOL (Istituto Ricerche Solari Locarno). For details concerning the observing procedure and reduction methods we refer to these papers and limit our presentation here to the features that are new or special to the present investigation.

### 2.1. Data set

The present paper deals with observations of the Stokes profiles of the Ca I 4227 Å line. While the circular polarization ( $V/I$ ) was recorded in addition to the linear polarization ( $Q/I$  and  $U/I$ ), we will only discuss the linear polarization results here, since the weak-field Hanle effect only affects the linear polarization. The Stokes  $V$  recordings were made for completeness, to monitor instrumental effects (like polarization cross talk), and to verify that the observations were made in quiet solar regions.

To take advantage of the minimum telescope polarization that occurs near the equinoxes, our observations were carried out during 5 days around the 1997 fall equinox, during 7 days around the 1998 spring equinox, and during one day near the 1998 fall equinox. The collected data set, after removal of the most noisy spectra (about 20% of the total), consists of 353  $Q/I$ , 353  $U/I$ , and 131  $V/I$  spectra. All recordings, except for 27 of them, were recorded in quiet regions. Examples of the 27 test recordings in active regions were presented and discussed in Paper III and will not be used here. Like Papers I and II the present paper deals exclusively with quiet regions.

The 4227 Å line has been observed in the 11th, 12th, or 13th grating orders, corresponding to different spectral fields of view (1.5 Å in the 13th order, 2.4 Å in the 11th order) covered by the

CCD sensor. We have checked whether the appearance of the polarized spectra depend on grating order and have not found such a dependence.

The typical exposure times were 10–20 s, and slit widths of 150 or 200 μm (corresponding to 1.2 or 1.6 arcsec on the Sun) were used.

Two CCD exposures are needed for each of Stokes  $Q$ ,  $U$ , or  $V$ . During the readout of a given frame the retarder is being rotated for the setting of the next frame. Each frame contains two orthogonally polarized spectra, and it is through the special combination of four such spectra (from two frames) that the fractional polarization ( $Q/I$ ,  $U/I$ , or  $V/I$ ) can be determined. To enhance the polarimetric accuracy we spatially average along the slit, which is oriented parallel to the limb, over a length of 15–18 arcsec.

### 2.2. Scattered light and polarization cross talk

All our data have been corrected for stray light in the spectrograph. This stray light has been determined by making recordings at disk center and comparing with corresponding FTS spectra recorded at Kitt Peak. The procedure for determining and correcting for the stray light is discussed in detail in Sect. 3.3 of Paper I. In the 1997 data we find stray light levels of 1.2–2% (as a fraction of the continuum intensity), while for the 1998 data the stray light is down at 0.5–0.7%. This decrease is the result of improvements, like cleaning of mirrors and better blocking of undesired light sources.

As in Papers II and III we find that the observations contain substantial cross talk from  $Q \rightarrow U$  and  $Q \rightarrow V$ . Cross talk in the opposite direction is unimportant here, because  $Q$  generally dominates over  $U$  and  $V$  in our data (since for the spatially smeared 4227 Å line in quiet regions it is the non-magnetic scattering polarization that dominates). The source of this cross talk (which was much larger than theoretically expected) has been discovered and eliminated. Due to a too thin aluminum coating of the third, flat telescope mirror, this mirror acted as a partial retarder. The mirrors have since been recoated, so that the telescope now behaves as it nominally should, but the data of the present paper were collected before this recoating. Nevertheless we could remove this cross talk problem in the data reduction process, as described in some detail in Paper II. The removal consists of subtracting some fraction of the  $Q/I$  spectrum from the  $U/I$  and  $V/I$  spectra, with the constraint that the intrinsic  $U/I$  and  $V/I$  polarization should approach a constant level in the distant line wings (where  $Q/I$  remains highly structured). As a second step the zero point of the polarization scale is shifted to make the constant level in the line wings zero (cf. Sect. 2.3 below). This procedure leads to good and consistent results.

Since the iron lines in the wings of the Ca I 4227 Å line are narrow and Zeeman sensitive, their polarization signatures allow us to make good cross talk corrections between the linear and circular polarizations. Let us however again point out that in the present paper we only analyse the linear polarization and do not deal with the circular polarization, which was always very small in the quiet regions studied here. The circular polarization in the

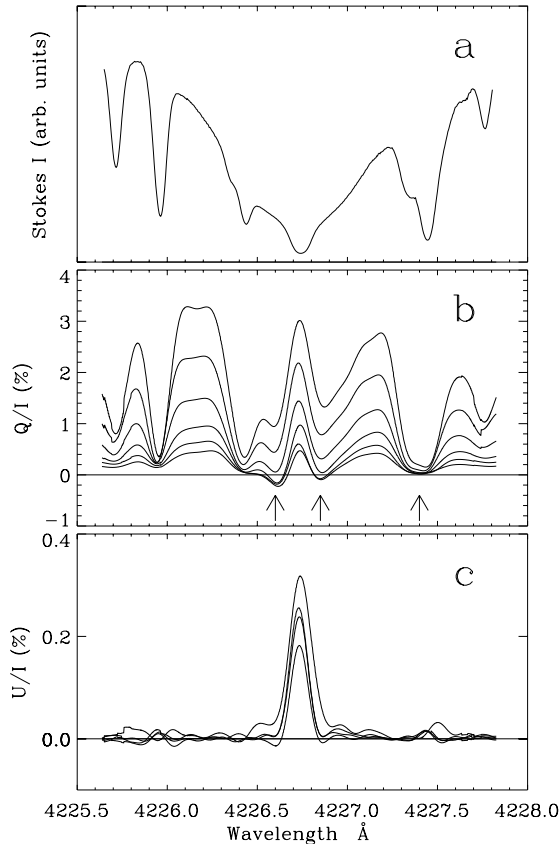


**Fig. 1a–c.** Examples of Stokes  $I$ ,  $Q/I$ , and  $U/I$  profiles of the Ca I 4227 Å line. **a** Stokes  $I$  profile at disk center. **b**  $Q/I$  profiles averaged over a sequence of  $\mu$  windows, to illustrate the center-to-limb variation. The arrows mark wavelengths referred to later in the text. **c**  $U/I$  profiles averaged over four of the  $\mu$  windows that were used in the  $Q/I$  panel. Only profiles with core amplitudes in excess of 0.05 % have been included in these averages.

Ca I 4227 Å line in active regions was discussed and compared with the linear scattering polarization in Paper III.

Fig. 1 gives examples of profiles of the intensity and linear polarization. The intensity profile in the top panel was recorded at disk center. The  $Q/I$  profiles in the middle panel illustrate the center-to-limb variation of the scattering polarization. They represent averages of individual  $Q/I$  profiles, after zero-level correction (see next subsection), within the  $\mu$  windows 0.0–0.1, 0.1–0.15, 0.15–0.25, 0.25–0.35, 0.35–0.45, and 0.45–0.55, respectively. As  $\mu$  represents the cosine of the heliocentric angle, the profiles for the smallest  $\mu$  (closest to the limb) have the largest amplitudes. The arrows mark wavelength positions that we will refer to later.

The bottom panel of Fig. 1 shows the  $U/I$  profiles that represent averages of individual profiles within the first four of the above-mentioned  $\mu$  intervals. For these averages only those  $U/I$  profiles that had an absolute core amplitude in excess of 0.05 % were used. Since both positive and negative  $U$  profiles occur (determined by the sign of the Hanle rotation angle), profiles with a negative core amplitude were first multiplied by  $-1$  before being used for the average.

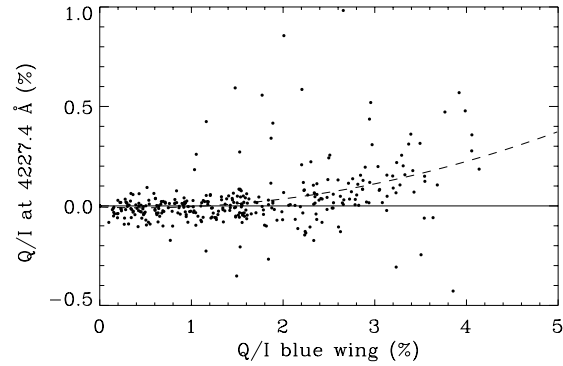


**Fig. 2.** Relation between the observed  $Q/I$  minimum at 4227 Å (marked by the right arrow in Fig. 1) and the  $Q/I$  maximum in the blue wing. The dashed curve is a second-order polynomial fit.

### 2.3. Polarization zero level

The observational zero level is nominally represented by the Stokes  $Q/I$  and  $U/I$  recordings at disk center, which should be intrinsically zero for symmetry reasons. The observational procedure is therefore always to alternate between limb and disk center recordings, such that the disk center spectra of the fractional polarization can be subtracted from the corresponding spectra elsewhere on the disk.

Although this procedure generally works well, there is a remaining scatter or uncertainty in the zero-level position, since the limb and disk spectra are not observed simultaneously. It is however possible to improve on this “preliminary” zero level to locate it more precisely. We do this by first examining the observed behavior of the values of the  $Q/I$  minimum at the wavelength near 4227.4 Å marked by the right arrow in Fig. 1b. They are plotted in Fig. 2 vs. the  $Q/I$  maximum in the blue wing (near 4226.2 Å), which is a well-defined function of limb distance or  $\mu$ . We assume that the scatter of the points is due to random errors in the zero level and have therefore made a least squares fit with a second-order polynomial to represent the true behavior of the minimum  $Q/I$  polarization near 4227.4 Å (dashed curve in Fig. 2). We notice that the points and the dashed curve approach zero for small values of the wing peak polarization, i.e., as we approach disk center.

It is now possible to find the true zero level, by subtracting from every  $Q/I$  profile the difference between the corresponding point in Fig. 2 and the second-order dashed curve. The profiles displayed in Fig. 1b have been corrected this way.

In the case of the  $U/I$  and  $V/I$  profiles the zero-level problem is much easier. We only have to assume that the mean value of the polarization far from the line center is zero and shift the observed profiles accordingly.

### 2.4. Determination of the limb distance

The slit is always oriented parallel to the nearest solar limb, and the limb distance defines the value of  $\mu$ . To compensate for image motions perpendicular to the solar limb a servo-controlled tilt-plate system is used for  $\mu$  values smaller than 0.3. The value

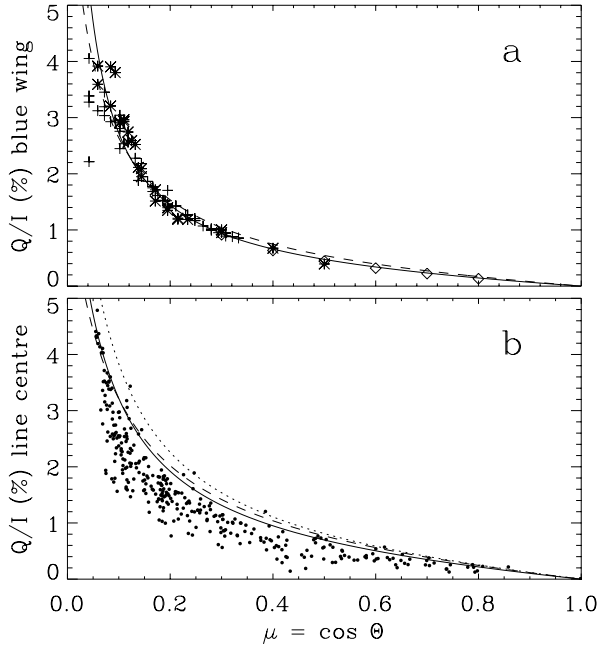


**Fig. 3.** **a**  $Q/I$  amplitude in the blue line wing, observed on three different days in 1998 (represented by the three symbols). The solid curve represents a fit with the function of Eq. (1), with the parameter values  $a = 0.33\%$  and  $b = 0.02$ . The dashed curve is the corresponding center-to-limb variation given in Paper I. **b** Center-to-limb variation of the  $Q/I$  amplitude at line center. The three curves represent envelopes based on the functional form of Eq. (1). The solid and dotted curves are the envelopes used in the later analysis.

of  $\mu$  is then determined from the reading of the tilt-plate sensor (read on the scale of the micrometer used to adjust the sensor). For  $\mu \geq 0.3$  (when the tilt plate is switched off) the limb distance is determined from the setting of the guider telescope.

Another method to obtain information on the  $\mu$  position would be to compare the alternating Stokes  $I$  profiles recorded near the limb and at disk center, while accounting for possible changes in the sky transparency. To convert such intensity ratios to  $\mu$  values we need to apply a center-to-limb curve, but such curves are well known only for the continuum, not for wavelengths inside the Ca I line. Since our spectral window is not wide enough to include a portion of the continuum, we are not able to use this method here to improve on our  $\mu$  values, only for more qualitative checks.

In our previous exploratory work on the  $Q/I$  polarization in the Ca I 4227 Å line in Paper I, an analytical expression from Stenflo et al. (1997),

$$\frac{Q}{I} = \frac{a(1 - \mu^2)}{\mu + b}, \quad (1)$$

was used with  $a = 0.4\%$  and  $b = 0.05$  to represent the observed  $Q/I$  amplitude in the blue line wing. To reexamine this relation with our present data set we select the three days that had the best sky transparency and therefore the smallest scatter in the determined  $\mu$  values (March 19 and 20, and September 21 in 1998). The blue wing maxima for these days are plotted in Fig. 3a with three different symbols for the three days. We

find that the earlier fit function is improved if we replace the old parameter values with  $a = 0.33\%$  and  $b = 0.02$ . The new fit is represented by the solid curve in Fig. 3a, the old fit (of Paper I) by the dashed curve.

Very close to the limb, for  $\mu < 0.075$ , we see considerable scatter in Fig. 3a, but we are presently unable to determine whether this scatter is of solar or instrumental origin, although it is most likely instrumental. Our polarimeter system is currently being equipped with an image rotator that will compensate for the image rotation of the Gregory telescope on the spectrograph slit. This will allow better control of the slit position near the extreme limb.

Magnetic fields do not contribute (via the Hanle effect) to the scatter of the points around the solid curve in Fig. 3a, since the Hanle effect has zero efficiency at the wavelength of the blue wing maximum. Assuming therefore that the solid curve represents the true center-to-limb variation of the  $Q/I$  blue-wing maximum and that the scatter of the points are due to errors in  $\mu$ , we can shift the points horizontally until they all fall on the solid curve. This method corresponds to inverting Eq. (1), using it to determine  $\mu$  from the observed  $Q/I$ . Since this method is almost independent of varying sky transparency, in contrast to the other methods, and since the noise in  $Q/I$  has a much smaller influence on the center-to-limb curves than uncertainties in  $\mu$ , we consider it to be the most accurate one, and have therefore adopted it to correct all our  $\mu$  values. The scatter around the linear relation in Fig. 4a below illustrates how small the noise in  $Q/I$  indeed is.

### 3. Analysis and results

#### 3.1. Hanle depolarization

Though the Hanle effect is always depolarizing for resonance scattering at  $90^\circ$ , it may lead to an increase of the linear polarization for certain field strengths and directions, when the scattering angle is different, as in the present observations. This effect, which was mentioned and briefly discussed in Paper II, increases when the scattering angle decreases. However, when the magnetic field has an unresolved structure like magnetic canopies or turbulent fields, the Hanle effect leads to depolarization for all scattering angles, due to the angular averaging over the highly non-linear Hanle effect. As our preliminary interpretation is only concerned with such unresolved fields, it will be self-consistent to assume a depolarizing behavior for the Hanle effect in the following data analysis.

Fig. 3b shows the  $Q/I$  amplitude at line center as a function of the center-to-limb distance parameter  $\mu$ . Here all the  $\mu$  values have been corrected with the blue-wing  $Q/I$  data as described above. They thus correspond to the case when the scatter of the points around the solid curve in Fig. 3a has been removed by adjustment of the  $\mu$  values. The scatter of the points in the diagram for the line-center (Fig. 3b) can be understood as due to Hanle depolarization (for the justification of this, see also Fig. 4 below). Since the Hanle depolarization works in the direction of reducing the polarization, the non-magnetic center-to-limb curve must lie above the points (if we disregard the instrumental

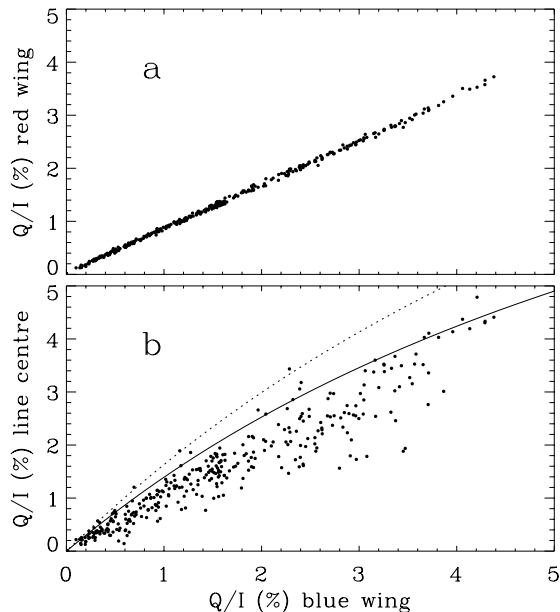


**Fig. 4a and b.** Red-wing **a** and line center **b**  $Q/I$  polarization amplitude vs. the  $Q/I$  amplitude in the blue line wing. The solid and dotted curves are obtained from the corresponding curves in Fig. 3b, using the solid curve in Fig. 3a for the relation between  $\mu$  and the blue-wing amplitude.

noise). The amount of depolarization, which is a function of the field strength, is given by the ratio between the observed polarization and the level of the non-magnetic curve for the same  $\mu$ .

The non-magnetic curve must be an envelope to the points in Fig. 3b, which we may represent in terms of the functional form of Eq. (1). The dotted and dashed curves represent the envelope choices made in Paper I, and correspond to the Eq. (1) parameter choices  $a = 0.6\%$ ,  $b = 0.055$ , and  $a = 0.6\%$ ,  $b = 0.085$ , respectively. Since the dashed curve intercepts the points for small values of  $\mu$ , we find it better to replace it with the solid curve, which has  $a = 0.52\%$ ,  $b = 0.06$ , and better represents a lowest possible envelope (accounting for the instrumental scatter). In the following we will use the solid and dotted curves as two possible envelope choices (to represent the non-magnetic center-to-limb variation).

Fig. 4 shows in the upper panel a scatter plot of the  $Q/I$  red-wing maximum vs. the corresponding blue-wing maximum, while the lower panel gives the line-center amplitude vs. the blue-wing maximum. As found for the corresponding plot in Paper I there is an excellent one-to-one correlation between the red and blue wings, while the linear polarization in the line core exhibits much scatter, as expected from the Hanle effect due to spatially varying magnetic fields. From the analytical expressions for the curves in Fig. 3, the solid and dotted envelope curves in Fig. 3b can be translated into the solid and dotted curves in the representation of Fig. 4b. The fractional distance (in the vertical direction) of the points from the envelope curves represents the magnetic-field induced Hanle depolarization.

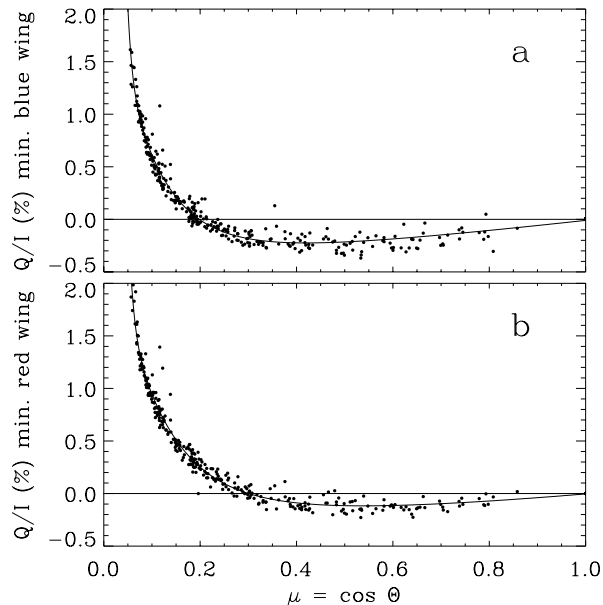


**Fig. 5a and b.** Center-to-limb variations of the  $Q/I$  minima on the blue **a** and red **b** side of the core peak. The solid curves represent 4th order fits as described in the text. Negative  $Q/I$  represents linear polarization oriented perpendicular to the solar limb.

### 3.2. Polarization oriented perpendicular to the limb

Since in the present work we have been able to accurately determine the zero point of the polarization scale, as described in Sect. 2.3 above, we are in a position to explore the detailed center-to-limb variation of the polarization minima around the core peak, at the wavelength positions marked by the left and middle arrows in Fig. 1b (the blue-wing minimum near 4226.6 Å, and the red-wing minimum near 4226.85 Å). They show the remarkable behavior of turning negative as we move away from the limb. For the blue-wing minimum this sign change occurs at  $\mu \approx 0.2$ , for the red-wing minimum at  $\mu \approx 0.3$  (cf. Fig. 5). Negative  $Q/I$  means that the plane of linear polarization is oriented perpendicular to the limb. From our analysis and control of the zero-line problem we conclude that this behavior cannot be instrumental but is of solar origin.

Since the wavelengths of the two polarization minima are located near the profile region where we have a transition between frequencies in the Doppler core and in the dispersion wings, it appears likely that partial frequency redistribution (PRD) plays a central role in generating the sign change, and that modelling of the center-to-limb curves in Fig. 5 requires that full account of angle-dependent PRD of polarized radiation is taken. This expectation is supported by the PRD calculations by Rees & Saliba (1982) and Saliba (1985), who have shown how the PRD physics indeed leads to a polarization maximum in the Doppler core, which is often surrounded by negative minima. The shapes of the polarized profiles depend on the details of both the chromospheric models and the PRD approximations used. We therefore expect the observed center-to-limb curves in Fig. 5 to be of considerable diagnostic use to constrain both the atmospheric models and to explore the details of PRD physics.

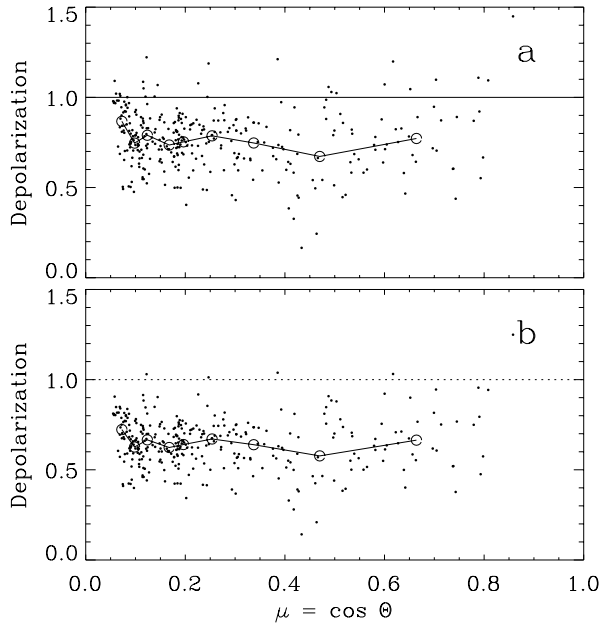


**Fig. 6a and b.** Values of the Hanle depolarization, determined as the ratio between the points in Fig. 4b and the two envelope curves. The top panel is based on the solid, the bottom panel on the dotted envelope curve.

The solid curves in Fig. 5 have been obtained by making 4th order polynomial fits to the  $Q/I$  minima vs. the  $Q/I$  blue-wing maximum, and then translating the blue-wing amplitude to  $\mu$ , using the previously found analytical relation (represented by the solid curve in Fig. 3a).

### 3.3. Field strength determinations

Fig. 6 shows the extracted values for the Hanle depolarization, determined from the line core data as the ratio between the points in Fig. 4b and the two envelope curves. Fig. 6a refers to the solid envelope curve, Fig. 6b to the dotted envelope curve (therefore the horizontal lines at depolarization unity have been drawn solid and dotted in the two panels). As depolarization values by definition should not exceed unity, the points that lie above this level may be considered as falling there either because of instrumental noise, or because the respective envelope curve in Fig. 4b has been chosen too low. However, some “spill-over” may be physically allowed (cf. Sects. 3.4 and 3.5).

To examine if there is any dependence on limb distance we have formed average values within  $\mu$  windows chosen so that each window contains 36 points. These average values are represented by the open circles, which are connected by straight lines. The standard deviation of the points around the mean values is between 0.1 and 0.2. Neither the mean values nor the standard deviations vary significantly with  $\mu$ .

We may now use the depolarization values in Fig. 6 to derive field strengths, in the manner that was described in detail in Sect. 4.3 of Paper I. As before, we use two models to describe the distribution of spatially unresolved magnetic field vectors: (a) The field vectors have a random distribution that is confined

to the horizontal plane (canopy field). (b) The field vectors have an isotropic distribution (turbulent field). Fig. 7 is obtained for these two models if we use the average depolarization values represented by the open circles in Fig. 6. The plus signs, which are connected by solid lines, are based on the solid envelope (the data in Fig. 6a), while the diamonds, which are connected by dotted lines, are based on the dotted envelope (data in Fig. 6b).

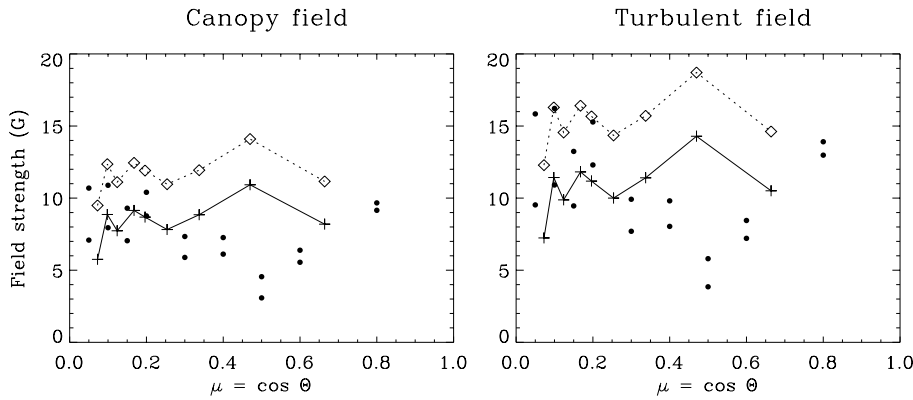
For comparison we have also plotted as the filled circles the field strengths derived for the Ca I line in Paper I. The agreement with the present data is good for small  $\mu$ , but the difference becomes fairly large for intermediate  $\mu$ , in particular around  $\mu \approx 0.5$ , where the old data have a minimum, while the new data have a maximum. We notice for instance in Fig. 6 that around  $\mu = 0.45$  some points have unusually small depolarization values, which corresponds to large values for the field strength. This can be partly due to the varying distribution of magnetic regions on the Sun (the observations of Paper I were made during a less active phase of the solar cycle).

Since there is no clear center-to-limb variation of the field strengths in Fig. 7, we may improve the statistics by using all the  $\mu$  values together and construct histograms for the distribution of the field strengths derived from each individual depolarization value in Fig. 6. For points that have “unphysical” depolarization in excess of unity (due to instrumental noise and/or incorrect choice of envelope), the field strength is set to zero (the value that one would obtain for a depolarization of unity). This artificially produces a maximum in the histogram for zero field strength, which becomes more pronounced when the lower envelope is used. This secondary zero-field maximum is thus most likely an artefact of the reduction procedure and not of solar significance.

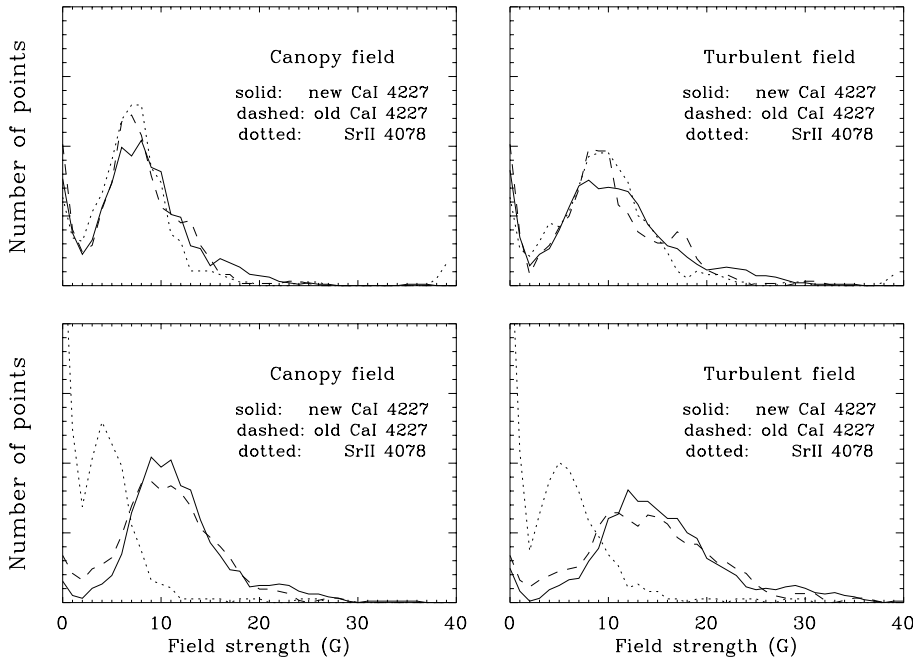
Such histograms were previously calculated for the Ca I 4227 Å data of Paper I and the Sr II 4078 Å data of Paper II and presented together in Fig. 2 of Paper III to compare the distributions obtained with the two spectral lines. In Fig. 8 we now compare the newly obtained distributions (solid curves) with the previous ones from the Paper I data (dashed curves) and the Paper II data (dotted curves). To facilitate the comparison between the distributions from the three data sets we plot the histograms in smoothed form, normalized to equal area. The panels to the left are based on the canopy field model, those to the right on the turbulent field model. In the two top panels we have used the lower envelopes for the Ca I data, the higher envelope for the Sr II data, while in the two lower panels the other envelopes have been used to derive the values of the field strengths.

Fig. 8 shows that there is excellent agreement between the distributions based on the Ca I line of the present data and those of Paper I. There is also an excellent agreement with the results for the Sr II line (Paper II) if for Ca I the lower envelopes are chosen and for Sr II the higher envelope, as shown by the two top panels of Fig. 8. However, all other combinations of envelopes result in smaller field strengths for Sr II as compared with Ca I. The particular choice of envelopes used in the upper panels of Fig. 8 would imply that the noise levels are substantially larger for Ca I than for Sr II, which is not the case.

An alternative interpretation could be that the Sr II 4078 Å line is formed somewhat deeper in the atmosphere, where the



**Fig. 7.** Field strengths derived from the average depolarization values (open circles in Fig. 6). The pluses are based on Fig. 6a, the diamonds on Fig. 6b, while the filled circles represent the results in Fig. 6 of Paper I. The left panel is based on a canopy field model, the right panel on a turbulent field model.



**Fig. 8.** Smoothed histogram distributions for the magnetic field strengths derived from the observed values of the Hanle depolarization. The solid curves are based on the data of the present paper (the points in Fig. 6), the dashed and dotted curves on the data of Papers I and II, respectively. The left (right) panels are based on the canopy (turbulent) field model. The top and bottom panels are based on different choices of envelope, as described in the text.

magnetic fields are different. The smaller field strengths in Sr II would then seem to imply that the field strength decreases with depth, which may appear counter-intuitive. There are however two effects that can lead to a decrease of the Hanle depolarization with depth: (1) The fields become increasingly more vertical with depth. The Hanle effect decreases and vanishes when the field inclination goes to zero. (2) The magnetic filling factor decreases with depth, if we only consider the flux tubes and disregard the contribution from turbulent magnetic fields. Only the fraction of the volume occupied by fields with a significant horizontal component can contribute to the Hanle effect.

### 3.4. Hanle rotation

If the directional distribution of the field vectors is not random within the spatial resolution element the Hanle effect may generate a Stokes  $U$  signal in the line core but not in the line wings, where the Hanle effect is absent. In Fig. 1c we saw examples of such observational signatures for the rotation of the plane of linear polarization due to the Hanle effect. If the angle of rotation

is  $\beta$ , then  $|\tan 2\beta| = |U|/Q$ . Fig. 9a shows a scatter plot of all the measured  $U/I$  amplitudes in the line core. For comparison the solid and dotted  $Q/I$  envelope curves from Fig. 3b are also plotted. In Fig. 9b we show the scatter plot of the  $|U|/Q$  ratio. The trend is that the relative number of points with large rotation angles tends to increase as we move away from the limb. Geometric foreshortening may produce such a trend, because the effective spatial resolution is lower towards the limb, so that we have less resolved fields and therefore smaller net rotation angles there.

Fig. 9 can be compared with the corresponding Fig. 7 of Paper II for the Sr II observations, which however did not extend beyond a  $\mu$  value of about 0.5, while our present data set for the Ca I line extends to  $\mu \approx 0.85$  and represents a larger statistical sample.

As in Paper II we next make scatter plots of the Hanle rotation vs. Hanle depolarization in Fig. 10 (which corresponds to Fig. 8 of Paper II). The Hanle rotation is represented by  $|U|/I$ , normalized to one of the  $Q/I$  envelopes of Fig. 3b. The amount of Hanle depolarization on the horizontal axis is represented by

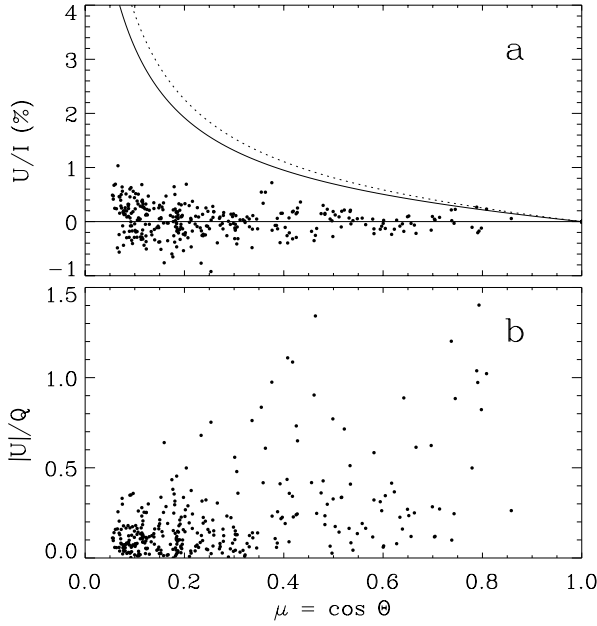


**Fig. 9a and b.** Scatter plot of  $U/I$  (top panel) and  $|U|/Q$  (bottom panel) vs. center-to-limb distance parameter  $\mu$ . The solid and dotted curves in the upper panel are the same as the solid and dotted  $Q/I$  envelope curves in Fig. 3b.

$1 - (Q/I)/\text{env.}$  (i.e., one minus the values in Fig. 6). Env. 1, used for the top panel, refers to the solid envelope curve of Figs. 3b and 9a, while env. 2, used for the bottom panel, refers to the dotted envelope curve in those figures.

To get a better feeling for these diagrams, we have in Fig. 10, as we did in Paper II, plotted the functions

$$y = \sqrt{x(1-x)} \quad (2)$$

as the solid curves, and

$$y = \sqrt{\frac{2}{3}x(1 - \frac{4}{3}x)}, \quad (3)$$

as the dotted curves. These curves represent the loci where the points would fall in the case of scattering at the extreme limb (approximating the  $90^\circ$  scattering case) when the magnetic field lies in the horizontal plane (canopy-type field). The solid curves correspond to the case when the magnetic field vector is directed towards the observer, while for the dotted curves the magnetic field is at an angle of  $45^\circ$  to the line of sight (assuming that the magnetic field orientation remains unchanged over the resolution element). The field strength increases from zero as we move along the curves from left to right.

Maximum Stokes  $U$  polarization (due to Hanle rotation) should occur when the magnetic field is along the line of sight. Therefore we would expect all points to fall below the solid curves in Fig. 10 in the case of this model, which refers to  $\mu = 0$ . The great majority of the points do indeed satisfy this expectation. The circumstance that some points in the diagrams scatter outside the region bounded by the solid curve may have different causes. One is the choice of the non-magnetic  $Q/I$  envelope, as we see by comparing the top and bottom panels of Fig. 10.

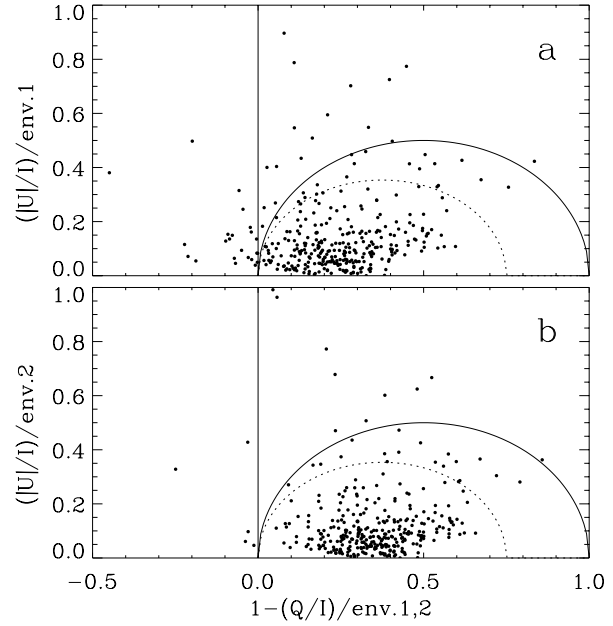


**Fig. 10a and b.** Scatter plot of Hanle rotation (here represented by  $|U|/I$ ) vs. amount of Hanle depolarization (represented by  $1 - (Q/I)/\text{env.}$ ). While the upper panel is based on the lower  $Q/I$  envelope (env. 1, solid curve in Fig. 3b), the lower panel is based on the higher envelope curve (env. 2, dotted curve in Fig. 3b). The solid and dotted curves are given by Eqs. (2) and (3), respectively, which are explained in the text.

Since the top panel is based on the lower of the two envelope choices, we find more points that scatter outside the bounded region as compared with Fig. 10b, which may suggest that the higher envelope choice is to be preferred. Another cause is of course instrumental noise, so we need to allow for some noise spill-over into the “forbidden regime”. However, the “allowed regime” expands into the previously “forbidden regime”, in particular towards negative values of  $x$ , as we go to larger  $\mu$  values, as was shown in Paper II (e.g. in Fig. 11 of Paper II). Therefore we should not interpret the solid curve as a definite, sharp boundary (since it is based on a simplistic model with  $\mu = 0$ ), but rather as an approximate tool to guide us in our overview of the data.

When there are unresolved magnetic fields with different orientations of the field vector within the spatial resolution element, there will be suppression of the  $U/I$  signal due to cancellation effects. This has the result that the distribution of  $U$  values tends to cluster towards a maximum near zero  $U$ , as evidenced by Fig. 10, where we find the majority of the points well below the dotted boundary, clustering towards the zero line for the Hanle rotation.

### 3.5. Hanle histograms

Since there is no clear correlation between the  $x$  and  $y$  values in Fig. 10, we may as in Paper II make separate histograms for the distribution of  $x$  and  $y$  values. Thus Fig. 11a shows the distribution of  $y$  values (representing Hanle rotation), while Fig. 11c

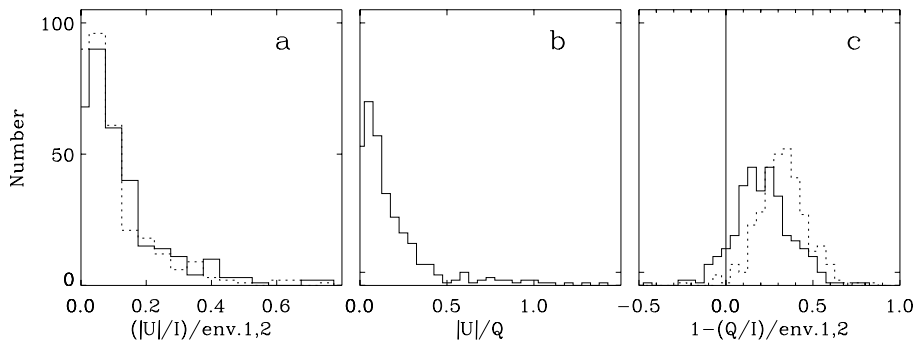


**Fig. 11a–c.** Hanle histograms, showing the distribution of the observed parameters representing Hanle rotation (panels **a** and **b**) and Hanle depolarization (panel **c**). Panel **a** represents the distribution of  $y$  values in Fig. 10, panel **b** the  $y$  values in Fig. 9b, panel **c** the  $x$  values in Fig. 10. The solid histograms are based on the lower (solid)  $Q/I$  envelope in Fig. 3b (env. 1), the dotted histograms on the upper (dotted)  $Q/I$  envelope in Fig. 3b (env. 2).

shows the distribution of  $x$  values (representing Hanle depolarization). Similarly, ignoring the possible, slight center-to-limb variation of the points in Fig. 9b, we have derived the distribution of the  $y$  values of that diagram ( $|U|/Q$ ) and plotted it in Fig. 11b.

The derived Hanle histograms in Fig. 11 are practically identical to those previously derived for the Sr II line in Paper II. Thus the parameters representing Hanle rotation (panels a and b in Fig. 11) show a distribution that monotonically increases towards smaller rotation values. The amount of Hanle depolarization, however, has a distribution with a maximum centered around a non-zero value. The location of this maximum varies between a depolarization ( $x$ ) value of 0.2 and 0.4, depending on the choice of non-magnetic  $Q/I$  envelope. The lower envelope choice (solid line) gives a distribution with more “spill-over” towards negative depolarization values. However, this does not necessarily imply that this envelope choice should be rejected, since somewhat negative depolarization values are physically allowed for non-zero  $\mu$  values (away from the extreme limb), and instrumental noise also contributes to such spill-over. In addition, radiative-transfer modelling by Faurobert-Scholl (1994) has shown that under certain circumstances, depending on the height of the magnetic canopy layer, the Hanle effect can enhance rather than diminish the polarization, which may also contribute to the “spill-over” in our diagram.

It is possible to calculate theoretical Hanle histograms from models of magnetic-field distributions, and then constrain these models by comparing the theoretical and observed histograms. Such a comparison was made in Paper II. As the present observational histograms are very similar to those of Paper II, we refer to this paper for details and limit ourselves here to summarizing the conclusions that can be made.

For the interpretation of the histograms we need to conceptually distinguish between two classes of magnetic fields: those that are spatially resolved, and those that are unresolved. Most observations correspond to the intermediate regime of partially resolved fields, but to elucidate the main features of the physical situation it is useful to assume that we can decompose the field into two distinctly separate components. Resolved fields then refer to the component for which the field vector can be considered to have constant strength and direction within the spatial resolution element. The spatially unresolved component will for the present idealized discussion be represented by fields that

have random orientations such that there is no net orientation when averaging over the resolution element.

With these definitions, if all the fields were spatially unresolved with no net orientation of the field, then there would still be Hanle depolarization, and Fig. 11c could be explained with the field-strength distributions that we actually derived in Fig. 8. However, this component would not contribute to any non-zero  $U$  values (Hanle rotation). The existence of an extended distribution of substantial Hanle rotation values (panels a and b in Fig. 11) can only be understood if there are contributions from (partially) resolved magnetic fields with a net orientation of the field vectors after averaging the contributions over the spatial resolution element. Contributions to this large-scale field component may come from the general, background magnetic field on the Sun, or from a canopy-type field that remains coherent over scales comparable to the supergranulation.

It is outside the scope of the present paper to try to derive more quantitative field-distribution models from the present Hanle histograms. Future observations with higher spatial resolution and with different spectral lines will help constrain the problem to enhance the diagnostic possibilities that the Hanle histograms offer.

### 3.6. Efficiency profile of the Hanle effect

According to theory the Hanle rotation and depolarization effects only occur in the Doppler core of spectral lines but not in their wings. In Paper II we could for the first time (for the Sr II line) empirically verify this property and determine the shape of the Hanle efficiency profile. Now we do this again for the Hanle rotation effect in the Ca I 4227 Å line. The procedure is the following: We collect all the observations within the  $\mu$  interval 0.10–0.25 for which we have recordings of both the  $Q$  and  $U$  line profiles, and for which the core peak value of  $|U|/I$  exceeds 0.12%. For these observations we then average the  $Q/I$  and  $|U|/I$  spectra and form the ratio between the averaged  $|U|/I$  and the averaged  $Q/I$  profiles. The result is plotted as the dashed curve in Fig. 12.

To compare the Ca I results with those of Sr II we have in Fig. 12 plotted as the dotted curve the Sr II efficiency profile from Fig. 13a of Paper II. Since we are here only interested in the relative profile shape, we rescale the dashed Ca I curve to get the solid curve that has the same amplitude as the dotted Sr II curve. The difference in amplitude between the dashed and

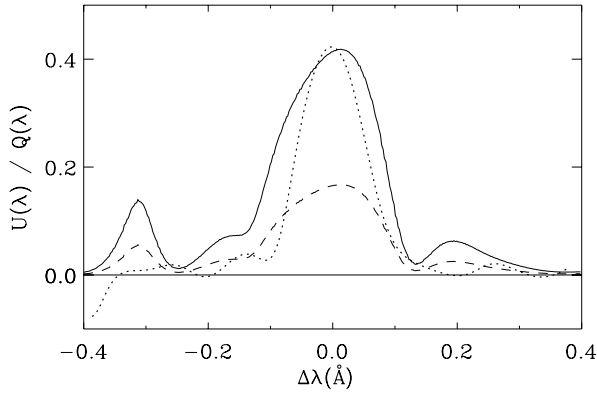


**Fig. 12.** Efficiency profiles illustrating how the Hanle effect is confined to the Doppler core of the line but vanishes in the wings. The dashed and dotted curves represent the average  $U/Q$  ratios in the  $\mu$  interval 0.10–0.25 for the Ca I 4227 Å line (from the present data) and for the Sr II 4078 Å line (from Paper II), respectively. The solid curve represents the dashed curve scaled to have the same amplitude as the dotted curve, to allow better comparison between the line widths. The side lobes of the solid and dashed curves are likely to be artefacts, because at these wavelengths  $Q/I$  is almost zero, which leads to great amplification of the instrumental noise in  $U/Q$ .

dotted curves is not of interest here, since it is only partly due to a real difference in the distribution of rotation angles. It is also to a significant degree due to the particular way that we selected the  $U$  and  $Q$  recordings to construct the corresponding  $U/Q$  profile in Paper II.

Our results for Ca I are consistent with the theoretical expectation that the Hanle effect operates in the Doppler core but vanishes in the wings. We also notice that the Ca I profile is broader than that of Sr II. This width difference is expected and of the correct magnitude. It has two main causes: (1) The larger thermal broadening for atoms with smaller atomic weight. This contribution to the width ratio scales with the square root of the ratio between the atomic weights 87.6 of strontium and 40.1 of calcium. (2) The wavelength difference. This contribution to the width ratio scales linearly with the wavelength ratio 4227/4078 for the two lines.

The side lobes seen in the wings of the Ca I profile in Fig. 12 are most likely due to instrumental noise, since they occur around the wavelengths, where Stokes  $Q$  is very small or even has a zero crossing, as seen from Figs. 1b and 5. Instrumental noise in  $Q$  will greatly magnify the errors in the  $U/Q$  ratio at places where  $Q$  is small. These places, and thus the spurious side lobes, should therefore be ignored in Fig. 12.

#### 4. Concluding remarks

In the present paper we have extended the exploration of the Hanle effect in quiet solar regions in the Ca I 4227 Å line that we began in Paper I by recording a large number of both Stokes  $Q$  and  $U$  profiles, which allows us to study the effect of Hanle rotation, to construct Hanle histograms for rotation and depolarization, and to determine the Hanle efficiency profile. A similar extension has been done in Paper II for the Sr II 4078 Å line. A

more complete comparison between the behavior of the Hanle effect in these two lines is therefore now possible.

We have in addition developed a special technique to determine the usually so elusive true zero point of the polarization scale, and have used this information to show how intrinsically negative  $Q/I$  polarizations (with the plane of linear polarization perpendicular to the limb) occur at certain places within the Ca I line profile, and how this intriguing polarization varies with center-to-limb distance (all the way to  $\mu \approx 0.85$ ). The explanation of these center-to-limb curves will be a future challenge for partial redistribution physics in polarized radiative transfer.

The comparison between the results in the Ca I and Sr II lines shows very good qualitative agreement, but there are also some indications of systematic, quantitative differences. As in our previous investigations with the Hanle effect we find that the field strength distributions peak approximately in the range 5–10 G, but the apparent field strengths found with the Sr II line tend to be somewhat smaller than those found with the Ca I line. As explained at the end of Sect. 3.3, a possible interpretation of this difference could be in terms of the height variations of the field inclination and filling factor, combined with the difference in height of formation of the two lines. There is also a tendency for the rotation angles to be smaller for the Ca I line as compared with the Sr II line.

The histograms of Hanle rotation and depolarization can only be consistently explained if there is a mixture of contributions from both partially resolved and unresolved fields with mixed orientations within the spatial resolution element. Since our present spatial resolution is quite low (on the order of 20 arcsec in the slit direction) because of the observational trade-off with polarimetric accuracy, it is not surprising that there is a major component of spatially unresolved magnetic fields of mixed orientations in our data, but it is also interesting that we with the present Hanle technique can diagnose the weak, large-scale component of the field as well. With increasing spatial resolution a larger proportion of the field structures can be resolved, and this can be expected to change the character of the observed Hanle histograms. We believe that this dependence on spatial resolution may have considerable diagnostic potential.

Ideally, it is therefore desirable to carry out the Hanle observations with the highest possible spatial resolution, for similar reasons as we need high spatial resolution in Zeeman-effect observations. Because of the weak signals involved, there will always have to be trade-offs between the polarimetric accuracy and the spatial, spectral, and time resolutions, even with the largest, future solar telescopes (cf. Stenflo 1999), but with increasing telescope aperture these scientific compromises will become less restrictive.

*Acknowledgements.* We are grateful for comments on the manuscript by Veronique Bommier, and for the financial support that has been provided by the canton of Ticino, the city of Locarno, and the ETH Zurich.

#### References

Bianda M., Solanki S.K., Stenflo J.O., 1998a, A&A 331, 760 (Paper I)

- Bianda M., Stenflo J.O., Solanki S.K., 1998b, A&A 337, 565 (Paper II)
- Bianda M., Stenflo J.O., Solanki S.K., 1999, In: Nagendra K.N., Stenflo J.O. (eds.) Solar Polarization. Proc. 2nd SPW, Kluwer, Dordrecht, p. 31 (Paper III)
- Faurobert-Scholl M., 1992, A&A 258, 521
- Faurobert-Scholl M., 1994, A&A 285, 655
- Povel H.P., 1995, Optical Engineering 34, 1870
- Rees D.E., Saliba G.J., 1982, A&A 115, 1
- Saliba G.J., 1985, Solar Phys. 98, 1
- Semel M., 1995, In: Comte G., Marcelin M. (eds.) 3D Spectroscopic Methods in Astronomy. ASP Conf. Ser. Vol. 71, p. 340
- Semel M., Donati J.-F., Rees D.E., 1993, A&A 278, 231
- Stenflo J.O., 1999, In: Nagendra K.N., Stenflo J.O. (eds.) Solar Polarization. Proc. 2nd SPW, Kluwer, Dordrecht, p. 1
- Stenflo J.O., Bianda M., Keller C.U., Solanki S.K., 1997, A&A 322, 985
- Stenflo J.O., Keller C.U., Gandorfer A., 1998, A&A 329, 319